AGU PUBLICATIONS

Geochemistry, Geophysics, Geosystems

RESEARCH ARTICLE
10.1002/2017GC007278

Key Points:
- First application of X-ray tomography to analyze zircon grain shape
- 3-D quantification of grain surface roughness and sphericity
- 3-D grain shape relates to source proximity, channel gradient and transport distance

Supporting Information:
- Supporting Information S1
- Table S1

Correspondence to:
V. Markwitz,
vanessa.markwitz@research.uwa.edu.au

Citation:
Markwitz, V., Kirkland, C. L., Mehnert, A., Gessner, K., & Shaw, J. (2017). 3-D characterization of detrital zircon grains and its implications for fluvial transport, mixing, and preservation bias. *Geochemistry, Geophysics, Geosystems*, *18*, 4655–4673. https://doi.org/10.1002/2017GC007278

Received 6 OCT 2017
Accepted 5 DEC 2017
Accepted article online 9 DEC 2017
Published online 26 DEC 2017

3-D Characterization of Detrital Zircon Grains and its Implications for Fluvial Transport, Mixing, and Preservation Bias

V. Markwitz[1], C. L. Kirkland[2], A. Mehnert[3], K. Gessner[4], and J. Shaw[3]

[1]School of Earth Sciences, The University of Western Australia, Crawley, WA, Australia, [2]Department of Applied Geology, Centre for Exploration Targeting – Curtin Node, John de Laeter Centre, Institute of Geoscience Research (TIGeR); Curtin University, WA, Australia, [3]Centre for Microscopy, Characterisation and Analysis, The University of Western Australia, Crawley, WA, Australia, [4]Geological Survey of Western Australia, East Perth, WA, Australia

Abstract Detrital zircon studies can suffer from selective loss of provenance information due to U-Pb age discordance, metamictization, metamorphic overprinting and fluviatile transport processes. The relationship between isotopic composition and zircon grain shape, and how grain shape is modified during transport, is largely unknown. We combine X-ray tomography with U-Pb geochronology to quantify how fluvial transport affects 3-D zircon shape, detrital age signature, and grain density along the Murchison River, whose catchment comprises Eoarchean to Early Paleozoic source rocks in Western Australia. We acquired tomographic volumes and isotopic data from 373 detrital zircons to document changes in size, shape and density in transport direction, and explore how grain shape, age spectra and the proportion of discordant material vary along the channel. Results show that shape characteristics are sensitive to transport distance, stream gradient, proximity to source material, and whether the source consists of primary or recycled zircons. With increasing transport distance, grain lengths decrease more than their widths. Furthermore, the loss of metamict grains occurs at a near constant rate, resulting in a linear increase of mean calculated zircon density by ca. 0.03 g/cm^3 per 100 km transport distance. 3-D grain shape is therefore strongly linked to detrital age signature, and mean grain density is a function of the absolute transport distance. 3-D shape characteristics provide valuable information on detrital zircon populations, including the interaction between source materials with fluvial transport processes, which significantly affects preservation bias and, by inference, the representativeness of the sampled data.

1. Introduction

Detrital zircon grains yield U-Pb ages and other geochemical proxies of source region (e.g., Hf isotopes), which are used to address a wide range of questions in the geosciences including identifying provenance, interpreting basin dynamics, quantifying growth of Earth's crust (e.g., Cawood et al., 2003; Kemp et al., 2010) and constraining the thermal evolution of its mantle (e.g., Voice et al., 2011). Zircon grains are resistant to many forms of weathering processes, including both chemical and mechanical abrasion, and are able to survive multiple cycles in a sedimentary system, as well as metamorphism (Fedo et al., 2003). Even though geochronology of detrital zircon is a powerful tool, the understanding of potential bias in the detrital population record is a fundamental challenge to its representativeness (Lancaster et al., 2011). Provenance information may be selectively lost due to U-Pb age discordance, metamictization and fluviatile transport processes. This selective loss affects the interpretation of how accurately the detrital record represents the growth and reworking of continental crust (e.g., Hawkesworth et al., 2009; cf. Gardiner et al., 2016). By sampling modern river systems, a bias related to selective bedrock sampling is avoided, as rivers erode large areas of exposed continental crust, including material that experienced prolonged sedimentary recycling and originated from various source rocks, which may not be exposed anymore (Iizuka et al., 2010). While the focus of many detrital zircon studies has been on the acquisition, analysis and interpretation of isotopic data sets, the relationship between isotopic composition and zircon grain shape, and how the grain shape is modified during transport, remains largely unknown. Although river sand samples are deemed representative of the bulk of zircon age distributions of continents (Condie & Aster, 2009), zircon size distributions and grain shape evolution are rarely considered for preservation bias. Only recently has it been shown

that the shapes of detrital grains carry provenance information and can contribute to the understanding of selective preservation (Markwitz & Kirkland, 2017; Shaanan & Rosenbaum, 2016).

Previous typological studies on magmatic zircon crystal habits have attempted to constrain grain shapes based on magma temperature and composition (Pupin, 1980). The occurrence of zircon fragments from highly fractionated magmas as opposed to pristine crystals may be related to metamictization processes, which cause weakening of the crystal structure and a decrease in grain density and hardness (Ewing et al., 2003). Thus, the degree of radiation damage can be related to surface texture changes from angular crystals to rounded and heavily etched grains. Furthermore, the elongation (length to width ratio, commonly between 1 and 5) of magmatic zircons may be a reflection of crystallization speed in the magma, with rapid crystallization producing needle-like grains in shallow-level and sub-volcanic intrusions, whereas short and stubby shapes are more common in deep-seated intrusions with slow cooling rates (Corfu et al., 2003). The shape of magmatic zircons can also be affected by zircon saturation of the magma: in highly fractionated magmas zircon saturation occurs well below the liquidus for differentiated members and zircon grains consequently fill interstitial spaces (e.g., Scoates & Chamberlain, 1995). Conversely, in zirconium-oversaturated magmas, crystals with sub-rounded to irregular shapes attain magmatic overgrowths. Irregular surfaces and shapes can also be the product of dissolution and precipitation during regional metamorphism and hydrothermal alteration (Corfu et al., 2003).

When eroded and transported in fluvial systems, detrital zircon grains are sorted based on their hydraulic behavior, hence detrital populations are likely to be controlled by size, density and original shape of individual grains (e.g., Garzanti et al., 2008). Grain size and shape are fundamental properties of sedimentary clastic particles, and the term "shape" can refer to a variety of attributes such as form, roundness and surface texture. Previous research on grain shapes in relation to river transport distances and depositional environments is biased toward an evaluation of quartz grains, where hydraulic behavior is interpreted from 2-D grain sections (Mazzullo et al., 1986). Several approaches have been used to characterize the shapes of sand particles and pebbles, including: Fourier series expansion, which describes a grain's roundness and texture (Wang et al., 2004), fractal analysis of roughness and size (Hyslip & Vallejo, 1997), calculation of grain sizes using 2-D grain sections (Cox & Budhu, 2008; Markwitz & Kirkland, 2017; Sircombe et al., 2001), wavelet analysis of grain size distributions (Buscombe, 2013), and the visual classification of heavy mineral surface textures under the microscope (Andò et al., 2012). One potentially important limitation of all these methods is the lack of 3-D quantification of key shape characteristics, as volume and surface area calculations are either extrapolations from 2D comparison charts (Pye & Pye, 1943) or derived from algorithms based on mathematical definitions of sphericity and roundness measures (Cox & Budhu, 2008). Whereas 2D studies rely on grain sections to infer size, textures, and surface characteristics, X-ray tomography (XRT) is capable of producing accurate 3-D representations of grain shapes and surfaces.

Here we present the results of the first X-ray tomography analysis of detrital zircon grains, which were subsequently analyzed for U-Pb isotopes by laser ablation-inductively coupled plasma mass spectroscopy (LA-ICP-MS), which allows an objective and quantitative 3-D grain shape characterization tied to the grains isotopic age. The objective of this study is to constrain 3-D grain shape evolution along the Murchison River in Western Australia, a large river channel that drains a catchment comprising source rocks with distinct age signatures. We show that the 3-D shape of detrital zircon grains is strongly dependent on transport distance, position in the channel network and proximity to source area, and that mean density of detrital grains relates to the absolute length of the channel. The shape of detrital zircon grains therefore carries meaningful information that can assist in evaluating preservation bias.

1.1. Geological Setting

The Murchison River catchment comprises Eo- to Neoarchean basement rocks of the Yilgarn Craton, Paleoproterozoic rocks of the Capricorn Orogen basins, Mesoproterozoic bedrock of the Northampton Complex (Pinjarra Orogen), and Phanerozoic sediments of the Southern Carnarvon Basin and the northern Perth Basin. Major regional faults include the Darling Fault, which separates the Yilgarn Craton from the Phanerozoic basins, and the Hardabut and Yandi faults that limit the outcrop of the Northampton Complex (Figure 1). Overall, the region is characterized by a low-relief landscape interspersed by topographic basement highs.

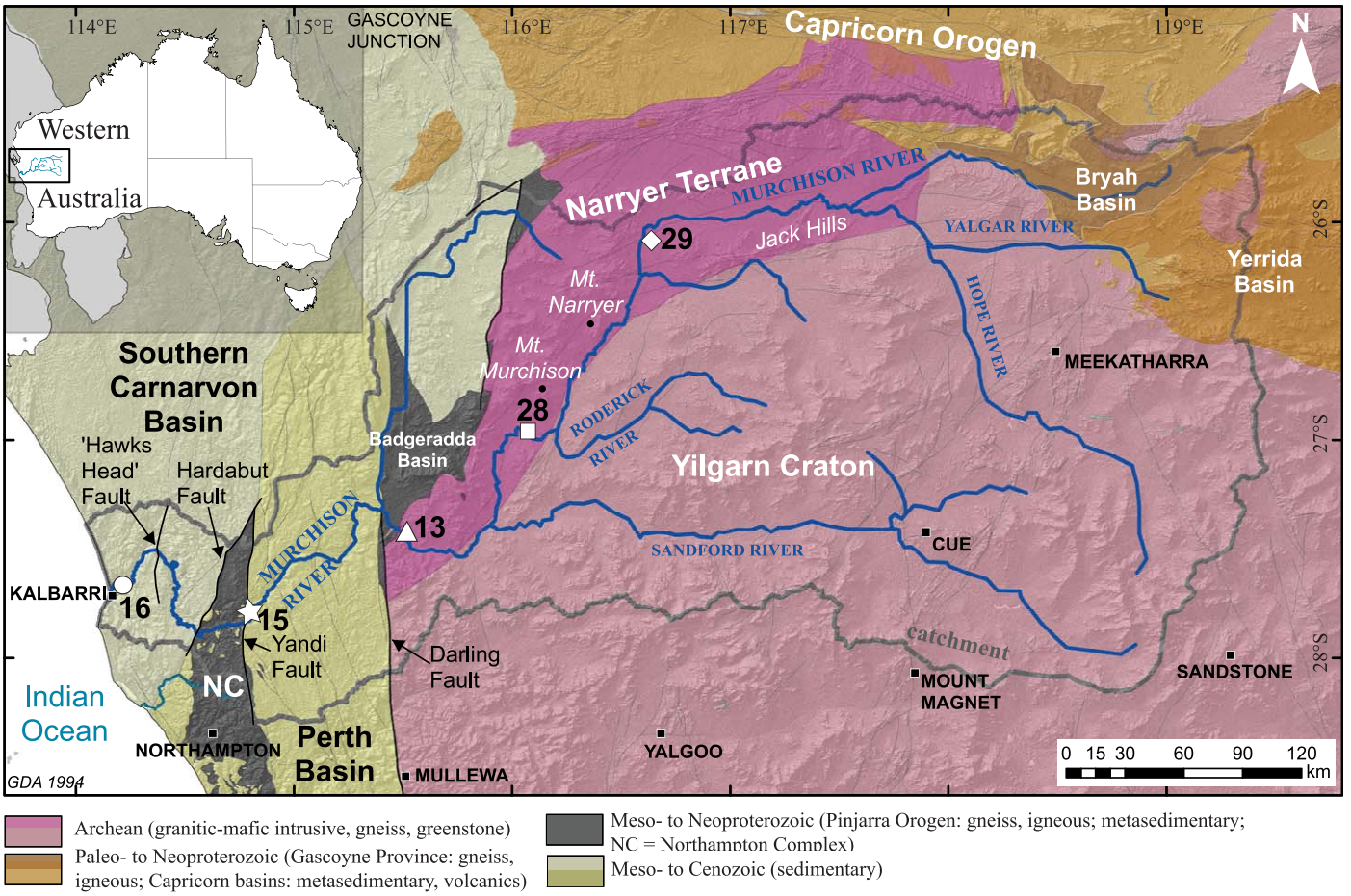

Figure 1. Geological map of the Murchison River catchment (grey outline) including sample locations (black numbers/white symbols) above a Digital Elevation Model (DEM) with Hillshade function.

The Yilgarn Craton consists mainly of Neo-to Mesoarchean granite-greenstone belts that formed between 2.6 Ga and 3.1 Ga (Champion & Cassidy, 2007), but also include >3 Ga granites, gneisses and metasedimentary rocks of the Narryer Terrane in the northwest of the craton, with evidence of 3.7 Ga tonalites (Griffin et al., 2004). The main channel of the Murchison River flows in close proximity to the ~3.6 Ga igneous source rocks near Mount Murchison (Sylvester et al., 2011), 3.5-3.7 Ga sources near Mount Narryer (Nutman et al., 1993) and along the Jack Hills greenstone belt, which includes Hadean detrital zircons (Wilde et al., 2001; see Figure 1 for location). The easternmost catchment of the Murchison channel system comprises Paleoproterozoic metasedimentary and volcanic rocks of the Capricorn Orogen, particularly from the 2.0 Ga Bryah Basin and the 2.2 Ga Yerrida Basin (Figure 1; Occhipinti et al., 2017; Pirajno & Occhipinti, 2000) that were deformed and metamorphosed during the 1.82 Ga to 1.77 Ga Capricorn Orogeny (Sheppard et al., 2003).

Outcrops within the northern Perth Basin and Southern Carnarvon Basin are isolated, except along the river profile of the Murchison River. The oldest sedimentary rocks are red beds of the Tumblagooda Sandstone that unconformably overlie the Northampton Complex and extend along the Murchison River Gorge and coastal cliffs south of Kalbarri (Hocking, 1987; McWhae et al., 1956). The Tumblagooda Sandstone comprises detrital zircon age populations spanning from 3.31 Ga to 0.46 Ga (Markwitz et al., 2017b). The Northampton Complex is part of the Mesoproterozoic Pinjarra Orogen and has experienced Neoproterozoic and Cambrian orogenies (Ksienzyk et al., 2012; Markwitz et al., 2017a). Detrital zircon ages from paragneisses of the Northampton Complex range from 2.04 Ga to 1.15 Ga (Bruguier et al., 1999), and the complex was subsequently intruded by 750 Ma dolerite dykes (Embleton & Schmidt, 1985). The flow of the lower Murchison River west of the Northampton Complex is characterized by stream knickpoints following prominent fractures that have been related to consistent uplift movements since the Eocene (Barnett-Moore et al., 2014).

1.2. Sample Selection

Five alluvium samples of approximately 5 kg each were collected from the main channel of the Murchison River (Figure 1) for 3-D grain shape analysis and U-Pb geochronology. These samples were used to determine morphological changes of grain surface area (roughness) and sphericity, determine age populations and apparent grain density, and calculate the relative rate of erosion (K). Three of the five samples (#29, #28, and #13) are from the Murchison's headwaters within the Yilgarn Craton, one from the northern part of the Perth Basin (#15) directly east of the Northampton Complex outcrops and one near the outlet (#16) in the Southern Carnarvon Basin. The sample locations were chosen to document the boundaries between craton and basin, and between basin and Northampton Complex.

2. Methods

The natural bias in the detrital zircon record is influenced by zircon durability and insolubility (Moecher & Samson, 2006) and other sources of bias may relate to radiation damage and associated U-Pb age discordance (Gehrels, 2014; Malusa et al., 2013). Sampling and mineral separation can have a significant effect on the representativeness of age spectra. As a result of hydraulic sorting, zircon age spectra within any given section of the channel can be significantly different (Lawrence et al., 2011). Bias can also be introduced by the selection of the sample site, and during sample preparation by preferential selection of grains during handpicking (Sláma & Košler, 2012). Further sources of bias may be introduced through magnetic separation of the heavy mineral fraction (Sircombe, 2000; Sircombe & Stern, 2002). A selection bias toward larger, pristine and clear zircon grains for analysis can be kept to a minimum by attempting to "randomly" select a large variety of grain sizes, colours and crystal habits. A minimum number of grains between 60–117 grains (Andersen, 2005; Dodson et al., 1988; Link et al., 2005; Vermeesch, 2004) should be analyzed in order to detect low abundance (3–5%) zircon age populations in detrital samples giving a 95% confidence level (Košler et al., 2013). We sampled, selected and processed all samples in a similar fashion to limit selection bias. All samples were taken from coarse to medium-coarse grained sands (Table 3) at the centre of the main channel to avoid bias by hydrodynamic fractionation of the zircon age populations. After multiple stages of sieving, the $>$1 mm fraction of the river sand samples was panned to concentrate heavy minerals. No magnetic separation was carried out. From the heavy mineral fraction of each individual sample approximately 150 zircons of assorted morphology, shapes and colour were handpicked. Zircons from each sample were mounted with zircon age reference materials in epoxy discs for scanning with the XRM Zeiss Versa 520 micro-CT at the Centre for Microscopy, Characterisation and Analysis (The University of Western Australia).

2.1. X-Ray Tomography and Image Analysis

2.1.1. Scanning and Reconstruction

Sample discs were individually secured in a bracket holder and scan parameters were optimized using the Scout-and Scan control system software (v10.6.2005.12038, Zeiss) of the Zeiss XRM. During scan time, an X-ray cone beam was focused on the disc containing the samples and data collected by a planar array of detectors. Grey scales reflect the relative X-ray attenuation coefficient, which is a function of density and atomic number (Ketcham, 2005). Following optimization, all samples were scanned using the following identical parameters. The source voltage and power was set to 60 kV and 5 W, respectively. A 2$\times$ binning was used and a 0.4$\times$ optical magnification (0.4$\times$ detector) to achieve an isotropic voxel resolution of 5.4 μm (source and detector to rotation axis distances $= -28$ and 329 mm respectively). The source filter was set to air. A secondary reference was collected using the LE6 filter for ring artefact reduction. Scans were run for 2001 projections through 360° with a 10 second exposure for each projection, giving a total scan time of approximately 5.5 hours per field of view. One of the original volumes of sample #16 is available for download (doi:10.4225/23/59d34351f9bce).Where sample size exceeded the field of view, multiple scans were performed and then combined using the Zeiss XRM vertical stitching procedure. Raw data were reconstructed using the Zeiss XMReconstructor software (v10.7.3679.13921, Zeiss) following a standard centre shift and beam hardening correction. The standard 0.7 kernel size recon filter setting was also used and the embedded LE6 secondary reference was applied. Reconstruction parameters were kept the same for all reconstructions.

2.1.2. Grain Segmentation

The grains were segmented (labeled) in each volume using a customized workflow developed in Avizo Fire 8.1.1 (www.fei.com) and presented in supporting information Table S1. The workflow essentially involves: (i) extracting a subvolume containing the sample of interest, (ii) 3-D filtering (curvature-driven diffusion) to attenuate noise, (iii) automatic threshold segmentation to identify voxels belonging to each grain, (iv) hole filling, (v) separation of touching grains and (vi) connected component labeling (Figures 2a–2d). The "Label Analysis" module in Avizo was used to extract the quantitative measures of grain size and morphology (referred to in italic typeface) described in Table 1. Detailed information about parameter choices and rationale is given in supporting information Table S1.

2.1.3. Quantitative Analysis of Grain Size, Morphology, and Roughness

A custom workflow was implemented in FIJI (image processing software; Schindelin et al., 2012) using the MorphoLibJ (Legland et al., 2016) plugin to smooth each grain in isolation by rolling spheres of increasing radii under and over the grain surface (conceptually a surface de-wrinkling filter). The filter is technically an alternating sequential filter (ASF) (Soille, 2013; Sternberg, 1986) comprising an opening followed by closing with a sphere of radius 1, then 2 and finally 3 voxels corresponding to neighbourhood sizes of ($3 \times 3 \times 3$), ($5 \times 5 \times 5$) and ($7 \times 7 \times 7$). The opening operation slides the sphere within a grain and sets to background those voxels for which the sphere cannot be admitted. Similarly the closing operation slides the sphere within the background and sets to foreground those voxels for which the sphere cannot be admitted. The effect is that progressively larger peaks and troughs are attenuated in the surface of a grain (a de-wrinkling or smoothing of the grain surface). We chose a value of 3 voxels to be able to characterize roughness on a scale of 5.4 μm. Given that the smoothing (curvature-driven diffusion) performed in the segmentation workflow influences the ASF, particularly for radius 1, we chose to define roughness as the surface area after application of the ASF divided by the surface area before. This is a relative rather than absolute measure. Furthermore, given that surface area measurements obtained by surface triangulation can be problematic (depends on the quality of triangulation) we chose to compute surface area directly from the voxel representation using a discretized version of the Crofton formula (Kiderlen & Meschenmoser, 2009) that computes intersections with line grids of various orientations (implemented in MorphoLibJ).

2.2. U-Pb Geochronology

After X-ray scanning for tomography, mounts were polished to half grain thickness, coated with Au and imaged with the Scanning Electron Microscope (SEM) at the Centre for Microscopy, Characterisation and Analysis (The University of Western Australia) to obtain cathodoluminescence (CL) images for laser spot selection. To ensure that this study is based on zircon grains only we used the SEM and the energy dispersive X-ray spectroscopy (EDS/EDX) to accurately map elements and analyze all grains from each sample. Polished, uncoated epoxy discs containing several samples each were analyzed with LA-ICP-MS (Resonetics RESOlution M-50A-LR sampling system, incorporating a Compex 102 excimer laser. Detailed information about the analytical set-up, standards and data processing is provided in supporting information Table S2) at the John de Laeter Centre (Curtin University, Australia). Zircon grains were ablated for 30 seconds at a 7 Hz repetition rate using a 33 μm beam spot (laser energy of 1.5 J/cm^2). A higher degree of discordance within the detrital data set can be a result of mixed sampling during ablation, which depends on zircon grain sizes and internal age structures. All data were reduced using the U/Pb Geochronology3 and trace element reduction schemes in Iolite^{TM} (Paton et al., 2011). Ages are reported with $\pm 1\sigma$ uncertainties calculated directly from isotopic ratios and filtered for concordance at a 10% discordance threshold; kernel density diagrams were generated by Density Plotter (Vermeesch, 2012). No common lead corrections were considered necessary due to low ^{204}Pb counts. Dates younger than 1,000 Ma are calculated based on the ^{238}U/^{206}Pb ratio; ages older than 1,000 Ma are calculated using the ^{207}Pb/^{206}Pb ratio.

3. Results

3.1. River Network Analysis of Catchment Area

We used a Digital Elevation Model based on the Shuttle Radar Topography Mission data (SRTM; Farr et al., 2007) as input into RiverTools (v. 3.0) to evaluate the Murchison River network. The results of the analysis are summarized in Table 2. With a maximal channel length of 1,265 km the Murchison River is the second longest river system in Western Australia. Its channel network extends from the southern edge of the Robinson Range 120 km north of Meekatharra, to the outlet at Kalbarri, where it enters the Indian Ocean

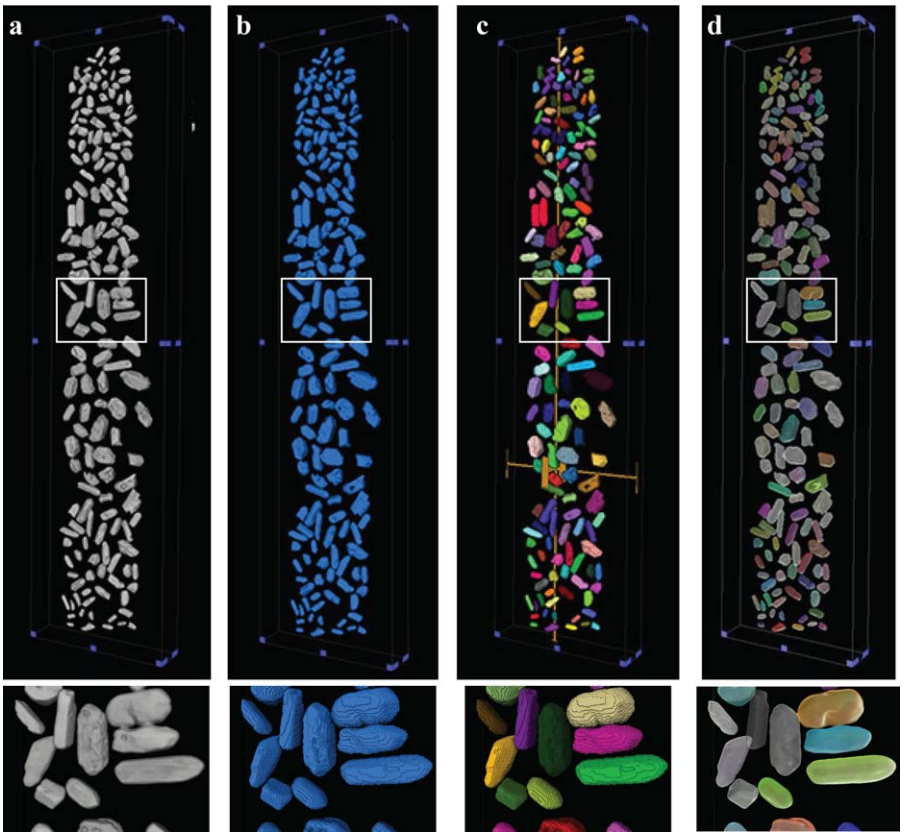

Figure 2. Grain segmentation workflow in Avizo. View of whole sample and enlarged detail below (white box): (a) Volume rendering of a 3-D volume reconstructed from X-ray tomography; (b) Binarization (auto-thresholding) and separation of grains; (c) 3-D connected component labeling (data probe is visible); (d) Transparent surface rendering of the grains.

(Figure 1). The catchment area consists of 1,03,325 km^2 semi-arid to arid bushland. Of the Murchison catchment (Table 2 and Figure 3a), 84% is underlain by Paleo- to Neoarchean basement rocks of the Yilgarn Craton and Paleoproterozoic rocks of the Capricorn Orogen basins, and 16% by Mesoproterozoic bedrock of the Northampton Complex and Phanerozoic basin sediments. The Murchison River network includes, from northeast to southwest, the Murchison, Yalgar, Roderick and Sandford Rivers (Figure 1). Across the Capricorn Orogen, the Yilgarn Craton and the basin region east of the Northampton Complex, the 1,146 km Yalgar-Murchison channel system elevation drops by 577 m along a smooth, graded profile within wide floodplain environment, resulting in an average channel gradient of 0.2 m/km. The correlation between slope and lithological changes is weak, and the Darling Fault has no topographical expression in the channel profile. In contrast, west of the Northampton Complex, several knickpoints and steeper river gradients that average 1.3 m/km are controlled by lithology changes along stratigraphic boundaries and faults. Features that stand out in the channel profile are the Hardabut Fault, which separates the Northampton Complex metamorphic rocks from sandstones of the Tumblagooda Sandstone, and an unnamed fault thereafter referred to as the "Hawks Head" Fault (Figure 1) that occurs within that sedimentary sequence. Between these faults the channel profile displays steep concave sections, which is consistent with the steep valley sides in the Murchison Gorge, where narrow channels cut through the Tumblagooda Sandstone. The distribution of elevation across the "Archean catchment" also shows a maximum between ca. 400 m and 500 m, which may point to the existence of an "ancient" peneplain in the Capricorn-Yilgarn portion of the catchment (Figure 3a–grey bold arrows; Figure 3b).

Table 1
Quantitative Measures of Grain Size and Morphology

Avizo measure	Description
Area3d	Surface area
Volume3d	Volume
Length3d	Maximum Feret diameter in 3-D
Width3d	Minimum Feret diameter in 3-D
Shape_VA3d	Dimensionless shape factor defined as Area3d^3/(36 x π x Volume3D^2); The quantity $\Psi = (1/\text{Shape\_VA3d})1^{/3}$ is called Sphericity[a], which is identically to 1 for a sphere and less than 1 otherwise

[a]Wadell (1935).

Table 2
Summary of River Network Analysis From the Murchison River Catchment Area

Murchison River catchment area	Sample ID	Elevation (m)	Channel distance to outlet (km)	Area of catchment (%)
Yilgarn Craton - Capricorn Orogen basins	29	332	663.21	84
	28	277	484.41	
	13	244	321.28	
Southern Carnarvon Basin	15	199	147.44	16
	16	2	2.40	
Major river systems	Max. elevation drop (m)		Channel length to outlet (km)	
Murchison River	556		1118.7	
Yalgar River	577		1,146	
Roderick River	440		690.6	
Sandford River	517		894.4	

Note. Max. basin area: 103325.42 km^2; max. basin relief: 10.65 km; longest channel length: 1,265 km; total channel length: 6,14,722 km.

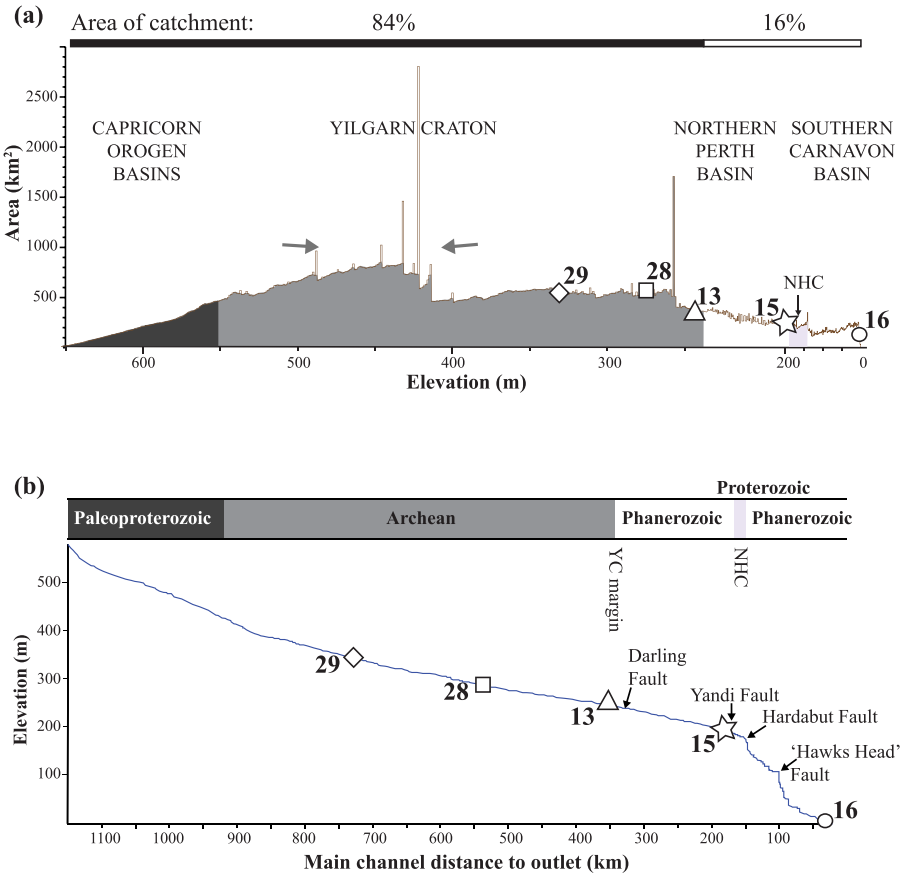

Figure 3. (a) Contributing area versus altitude of the Digital Elevation Model (DEM) highlighting the proportion of catchment area and the proportional change in area along the river transport of the Murchison main channel. The numbers refer to sample locations. A maximum between ca. 400–500 m (grey bold arrows) indicate to the existence of an "ancient" peneplain in the Capricorn-Yilgarn portion of the catchment. Spikes in the plot correspond to the contour interval of the DEM, with a bin value of one metre. NHC = Northampton Complex. (b) Longitudinal channel profile from the main channel of the Murchison River.

3.2. Geochronology

Detrital zircon U-Pb ages are displayed in combined probability density plots and Tera-Wasserburg concordia diagrams in Figure 4. A total of 373 U-Pb analyses were performed of which 170 concordant ages (<10% discordance) across all five sample locations were recovered (Table 3 and supporting information Table S3). The high proportion of discordant data reflects analyses from metamict grains with a high U content (averaging 1,091 ppm). This U content contrasts with grains that yield concordant ages, which have an average of 378 ppm U (supporting information Table S3). The proportion of discordant data changes with transport distance: Yilgarn Craton river sands contain up to 68% discordant data, compared to 46% in the basins. The degree of metamictization and apparent density in the detrital zircon population was determined by the calculation of the dose of α-events for each grain by using U and Th concentrations and $^{206}Pb/^{207}Pb$ ages (after Murakami et al., 1991). Calculated apparent densities of zircon grains show a continuous increase in mean value from 4.17 to 4.64 along the transport pathway (Table 3 and supporting information Table S3), indicating a density change from moderate to highly dense crystals downstream from the Archean craton.

Detrital zircons show a typical range of subhedral, elongated prisms with short pyramidal endings to stubby round crystal faces and grain fragments. Few grains exhibit clear oscillatory zoning in CL images, whereas most display patchy internal structures with relatively homogenous CL responses. Three samples located within the Narryer Terrane of the Yilgarn Craton (#29, #28, #13; see Figure 1 for location; Table 3) contain dominantly Archean age signatures ranging from 3,541 Ma to 2,613 Ma, with minor Paleoproterozoic age components from 2,023 Ma to 1,994 Ma. Samples located in the basins (#15, #16) carry different proportions of Archean ages (Figure 4), with 74% Archean zircon in sample 15 (located east of the Northampton Complex) and 35% near the rivers outlet (#16). Sample #16 contains significant Proterozoic and Paleozoic age peaks from 3,056 Ma to 486 Ma and sample #15 from 3,440 Ma to 518 Ma.

3.3. 3-D Grain Shape Analysis

3.3.1. Grain Size

Grain size distributions in river sands vary between sample locations and transport distances (Table 3). Samples from the Yilgarn Craton (#29, #28, and #13) carry the largest grain lengths of up to 805 μm whereas multi-cycle basin samples (#15, #16) have maximum lengths of 689 μm (Table 3). Overall, sample #15 contains the smallest detrital zircon grains with a maximum length of 246 μm compared to sample #16 further downstream with length up to 689 μm.

3.3.2. Grain Sphericity

Sphericity (ψ) provides a quantitative measurement of roundness by considering a ratio between surface area and volume of an object (Table 1). As a benchmark for zircon grain sphericity, we generated five virtual zircon shapes using the morphology program WinXMorph (Kaminsky, 2007; Figure 5a) and measured sphericity in Avizo. These virtual zircons were chosen to represent common combinations of the prims and pyramid faces in magmatic zircon (Corfu et al., 2003), the most common genetic type of zircon at source. These five virtual grains range in sphericity between 0.64 and 0.95, with a mean of 0.81 (standard deviation: 0.09).

Detrital zircon grains in our study area range in mean sphericity between 0.869 in the upstream catchment area to 0.894 east of the Northampton Complex (Figure 5b and Table 3). Grains with the highest sphericity occur in sample #15 east of the Northampton Complex. In the direction of river transport, grain sphericity continues to decrease toward the outlet of the Murchison River. In Yilgarn Craton samples, grain sphericity values are generally lower than in the basin samples, exhibiting irregular grain morphologies and less grain rounding.

3.3.3. Grain Roughness and Pitting

We measured roughness of 373 zircon grains to evaluate the degree of damage (e.g., pitting and fragmentation) related to transport distance and ages (Figure 5b and supporing information Table S3). The roughness of grains is a consequence of damage textures, and includes (1) smooth shallow depressions; (2) uniform shallow pits, concave prism faces, or shallow linear marks; (3) irregular narrow pits, large dents across the grain, and deep pits (Figures 5c and 5d). The morphology of deep pits is illustrated in Figure 5c. We recognize that the shape and size of the pits are highly variable and include tube-like funnels that follow no apparent lattice direction and can branch out or widen within the grain.

In general, the variations in roughness measures are subtle in between samples, but the data range is considerable and mean values show important differences, which highlights the degree of pitting, linear

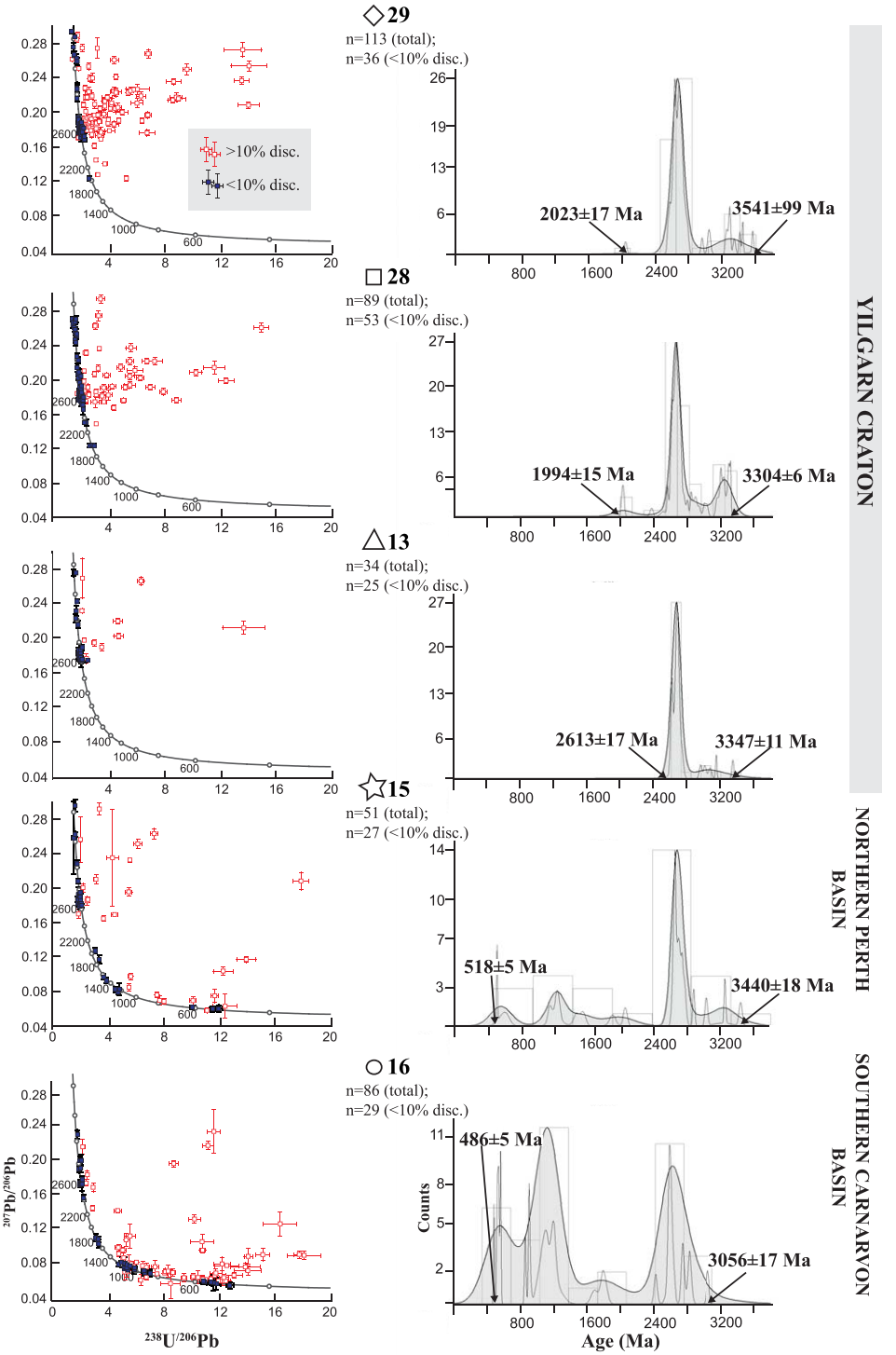

Figure 4. Left column: Tera-Wasserburg plots with 1σ error bars (concordant data in dark blue; discordant in red) for all samples taken along the Murchison channel system. Right column: probability density diagrams (black line) combined with kernel density estimations (grey shaded areas) and histograms (grey rectangles) derived from concordant data. The calculated minimum and maximum detrital zircon ages for each individual sample are noted in bold typeface; symbols of samples as in figure 1 and 3.

Table 3
Sample Locations, Proportion of Discordance Data, Main Age Peaks, Mean Apparent Density and Summary Statistics for Detrital Zircon Grain Size, Sphericity and Roughness Measures for Individual Samples

Sample ID		29	28	13	15	16
Lat. / Long.		−26.094 / 116.617	−26.977 / 116.047	−27.435 / 115.510	−27.817 / 114.777	−27.696 / 114.171
Grain size		Coarse sand	Coarse sand	Coarse sand	Coarse sand	Coarse-medium sand
(volume weighted mean - phi)		(0.49)	(0.38)	(0.44)	(0.9)	(1.1)
Total number of ages / <10% disc. analyses		113 / 36	89 / 53	34 / 25	51 / 27	86 / 29
Proportions of >10% discordant ages (%)		68.46	39.32	27.27	46	66.26
Main age peaks (number of grains)		2,643 Ma (9); 2,685 Ma (8); 2,586 Ma (4); 2,764 Ma (3); 3,292 Ma (3)	2,663 Ma (14); 2,611 Ma (8); 3,227 Ma (5); 3,279 Ma (4); 2,835 Ma (3); 2,887 Ma (3); 3,189 Ma (3)	2,683 Ma (12); 2,620 Ma (7); 2,737 Ma (3)	2,658 Ma (8); 2,702 Ma (6); 2,740 Ma (4)	1,101 Ma (6); 2,606 Ma (5); 907 Ma (3)
Age range (Ma; ≤10% disc.)		2,023–3,541	1,994–3,304	2,613–3,312	518–3,228	486–3,056
Apparent density (mean; g/cm^3)[a]		4.17	4.25	4.39	4.47	4.64
Apparent density (mean; g/cm^3)[b]		4.69	4.70	4.72	4.72	4.74
Length3d	Range	111–805	129–457	182–449	91–264	97–689
(μm)	Median	247.34	288.66	272.93	149.30	228.73
	STD	89.92	73.57	65.85	42.67	83.42
Width3d	Range	84–384	66–233	77–242	59–152	68–311
(μm)	Median	123.11	152.74	125.87	84.94	133.15
	STD	41.34	33.15	33.46	18.73	50.45
Sphericity	Range	0.739-0.945	0.797-0.980	0.801-0.937	0.800-0.983	0.743-0.966
	Median	0.860	0.885	0.853	0.917	0.893
	STD	0.04	0.03	0.03	0.04	0.04
Roughness	Range	0.024-0.036	0.029-0.037	0.029-0.035	0.017-0.070	0.028-0.033
	Median	0.0313	0.0320	0.0320	0.0308	0.0322
	STD	0.001	0.0006	0.0009	0.006	0.001

Note. STD = Standard Deviation.
[a]After Murakami et al. (1991).
[b]Recalculated with a 500 Ma cooling age.

denting and marks on grain surfaces. There is a significant relationship between grain roughness and transport pathway. Yilgarn Craton river sand samples contain grains with higher mean roughness than basin samples (Table 3 and Figure 5b). Overall, the detrital zircon grains from #28 display higher surface roughness values than grains from #29, whereas roughness in #13 shows an overall decrease in values with smoother surfaces. Similar to a downstream increase in sphericity of zircon grains from #13 to #15, grain surface roughness values decrease and grains exhibit less pitting and denting. An increase in roughness from #15 to #16 can be explained by the introduction of larger, more dented zircon grains from additional proximal sources of the Northampton Complex. This suggests that grain roughness is, to a large extent, a primary attribute of the grains in their source rocks as a consequence of magmatic, metamorphic or metasomatic processes.

4. Discussion

4.1. Murchison Channel Network and Catchment

Modeling the channel slope shows that shallow river gradients persist from the headwaters of the Murchison River across the Darling Fault into the basins, where floodplains increase in width. Although the Darling Fault is very long and has considerable stratigraphic and tectonic significance, it has no expression in the longitudinal channel profile (Figure 3b). This is consistent with the lack of evidence for historical seismicity and tectonic displacement on this structure during the Quaternary (Jakica et al., 2011). Prominent stream knickpoints, followed in the downstream direction by convex channel profiles, are located at the Hardabut Fault west of the Northampton Complex and the "Hawkes Head" Fault, which points to a strong structural

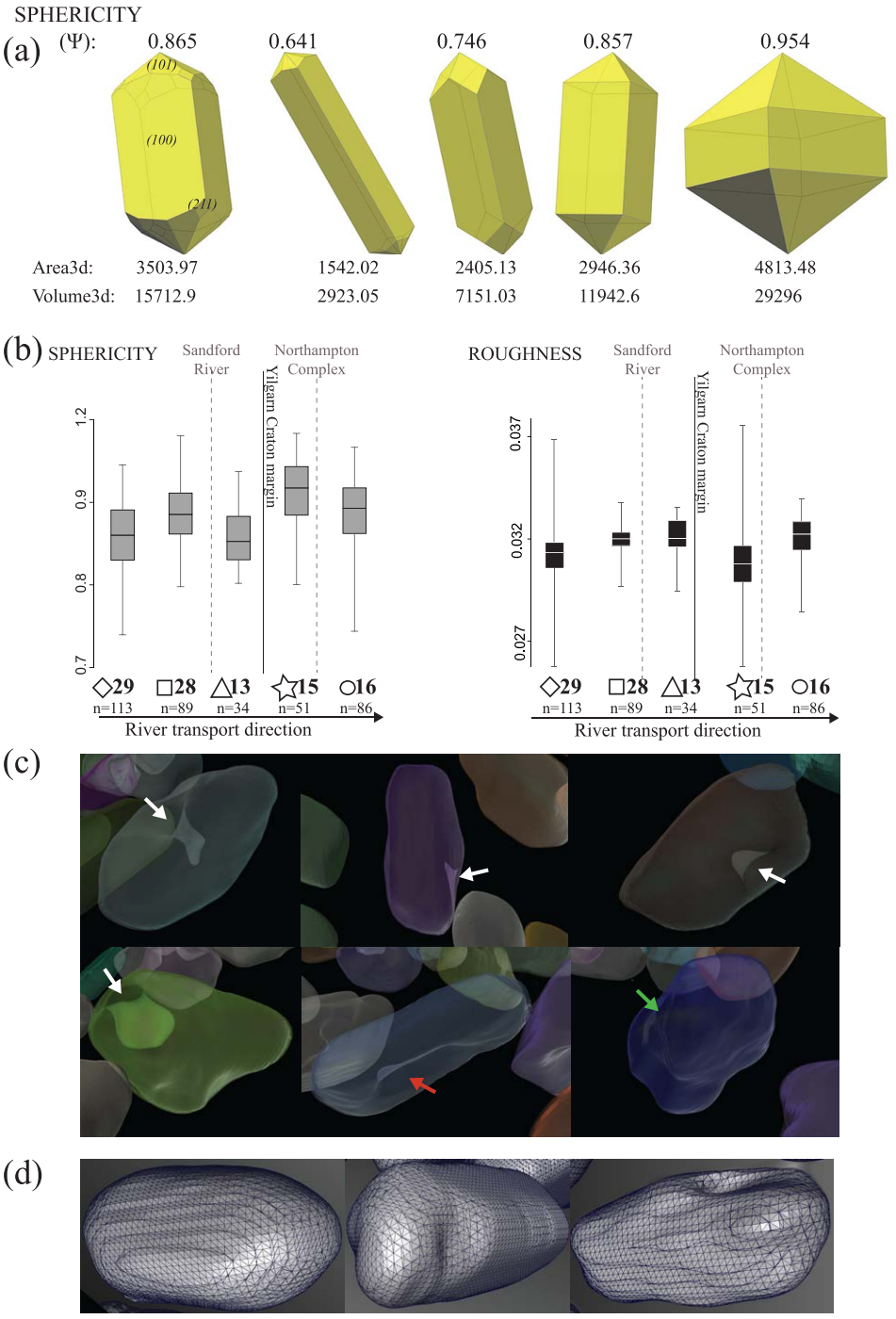

Figure 5. (a) Sphericity (ψ), surface area (*Area3d*) and volume (*Volume3d*) calculated in Avizo for five virtual zircon models with morphologies determined by common crystal faces (pyramids {101} and {211}; prisms {100} and {110}). *Area3d* and *Volume3d* are Avizo shape measures. 3-D surface characterization of detrital zircon grains. (b) Box plots of grain sphericity (Ψ) and roughness in transport direction displaying the median value and the interquartile range as a vertical bar (box). (c) 3-D visualization of detrital zircon grain surfaces: transparency highlights pit morphologies (white arrows), linear dent (red arrow) and a typical irregular surface (green arrow). (d) Meshed surface models of detrital zircon grains representing the three levels of roughness (from left to right): (1) smooth; (2) uniform shallow pits, concave prism faces, shallow linear marks; (3) irregular narrow pits, large dents across grain, and deep pits.

control of the drainage in the vicinity of the Murchison Gorge, where tightly bending channels that follow prominent fractures cut through steep river banks. Virtually all first order streams in the Murchison Gorge are incised along major joint surfaces and fractures, which control the erosion (Young, 1986). These surface characteristics are consistent with the cumulative uplift history of this region that has occurred since the Eocene, with a maximum uplift recorded in the Mid-Neogene (Barnett-Moore et al., 2014).

4.2. Erosional Bias and Detrital Load

Yilgarn Craton river sand samples (#29, #28, and #13) contain mainly detritus from proximal Archean source material with minor age components from the more distal Paleoproterozoic Capricorn Orogen basins (Figure 6a). The introduction of large quantities of source material at the Sandford River confluence changes the detrital population in #13 into 100% Archean ages, probably by "diluting" the remaining Paleoproterozoic age fraction below detection. Basin samples in comparison contain more age components, including Archean, Proterozoic and Paleozoic. An increase of Meso-Neoproterozoic age populations from basin sample #15 to #16 is likely due to the addition of new source material from the Northampton Complex.

In order to quantify any potential erosional bias and its influence on the detrital zircon signature an age-based erosion parameter "K" (Allègre & Rousseau, 1984) can be calculated, which represents the age proportions of the source material (%Source) in a sediment relative to the age proportion of source material (%Basin) in the overall catchment area:

$$K = [(\%\ \text{Basin})/(\%\ \text{Source})]\mathit{Sediments}/[(\%\ \text{Basin})/(\%\text{Source})]\mathit{Source} \quad (1)$$

K gives insights into the proportions of detritus that are lost during transport, but also reflects selective erosion and sediment supply from areas of greater topographic relief. The erosional bias increases with transport distance, e.g., from the Capricorn - Yilgarn portion of the catchment to the outlet and is a function of the river's gradient (Figure 6a). The overall catchment area consists of 84% Archean Yilgarn Craton, yet the craton contributes only 35% of the detritus near the outlet of the Murchison River (Figure 3a). Based on our river network analysis, an overall low stream gradient of ca. 0.5 m/km results from an elevation change of 332 m over a distance of 663 km (Table 2). $K = 1$ represents no preferential erosional bias for river sands of the Yilgarn Craton region (Figure 6a), with a calculated gradient of 0.257 m/km. Between #13 and #15 the river gradient remain constant (0.258 m/km) and K slightly increases to 2, which documents the differences in age spectra. The slope from the Yilgarn Craton into the basin east of the Northampton Complex is relatively shallow and gentle (Figure 3b). Conversely, the relief changes considerably as the lower Murchison River passes through the Murchison Gorge. Between Hardabut and "Hawks Head" Faults, the relief and gradient changes to 1.366 m/km with an increase of $K = 7$ (Figure 6a). The increase in gradient has resulted in the additional exposure and erosion of Northampton Complex material and Paleozoic Tumblagooda Sandstone, which have a clear effect on the age population range in sample 16 (Figures 3a and 6a). The river sands in the Murchison Gorge are dominated by "younger" sources that are eroding locally, therefore the Archean age component appears to be diluted.

The increase of the K value in relation to river gradient steepening is illustrated by a change from $K = 2$ (upstream from Northampton Complex) to $K = 7$ (outlet), which coincides with a fivefold increase in channel slope. All low K values, between one and two, coincide with flat channel profiles with low gradients, and represent a mature river system that drains the Yilgarn Craton with characteristically wide shallow channel systems and large floodplains. The constant removal of the Archean zircon population along the transport direction is likely due to the loss of metamict grains and mixing of zircons with contrasting provenance from the Greater Yilgarn Craton, Capricorn Orogen basins, Northampton Complex and Greater India (the Tumblagooda Sandstone; Markwitz et al., 2017b).

4.3. 3-D Grain Shape of Detrital Zircon

This is the first study to use X-ray tomography to document and quantify the 3-D shape of detrital zircon grains in a modern river system. Using the tomographic volumes and their surfaces allows us to identify strong links between grain roughness, river transport distance and proximity of source regions, which is comparable to the degree of sphericity changes in the grains (Figures 5b and 6b). Our results from sphericity and roughness calculations illustrate the relationship between transport distances, proximity to source material and sample location. Detrital zircons have a median sphericity of 0.882 across all samples (Table 3). The sphericity of detrital grains depends on sample location and source regions, and distance along the

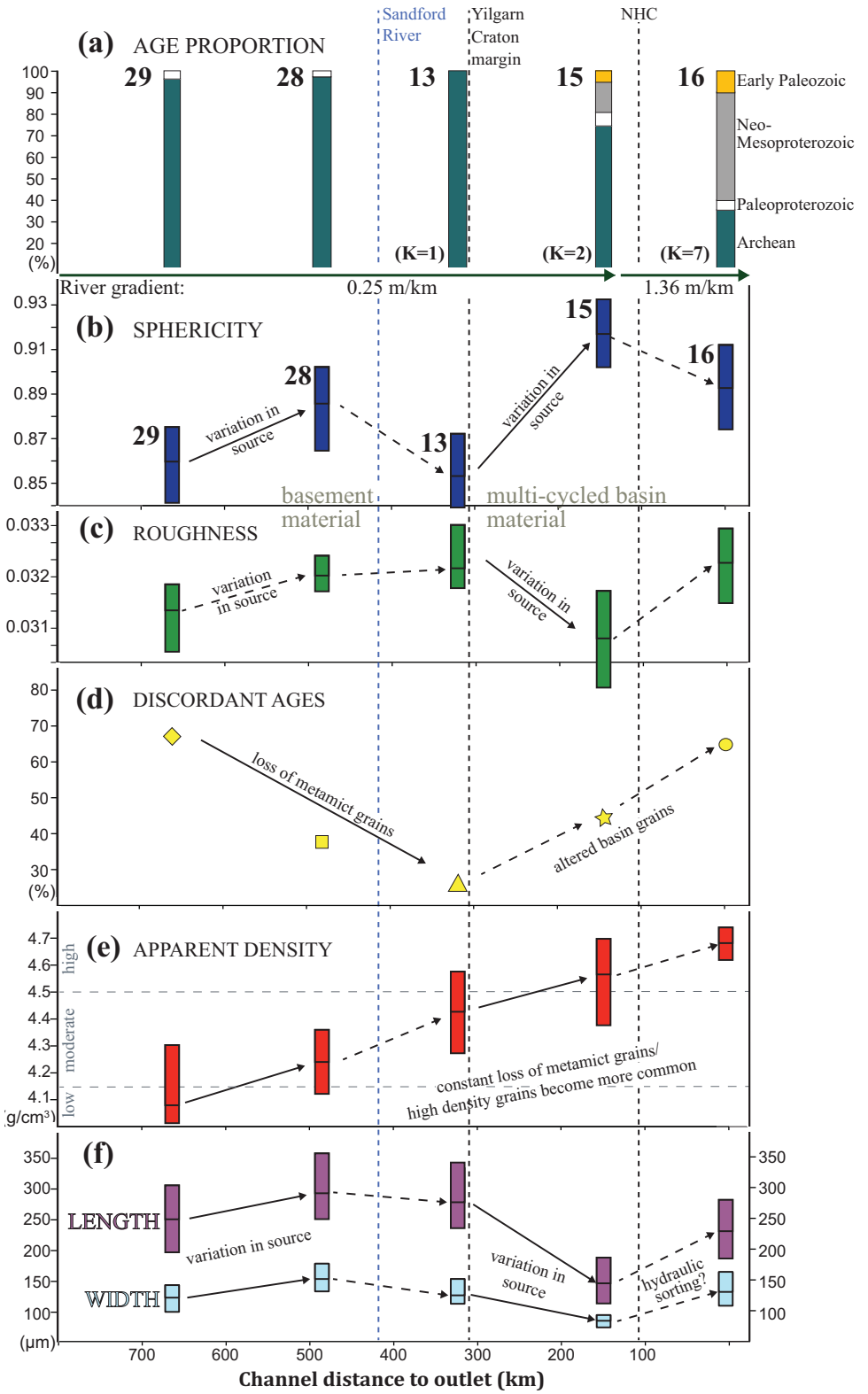

Figure 6. Grain shape and size variations along fluvial transport direction. Dashed lines indicate source changes. (a) Proportions of zircon age groups for each sample with corresponding erosional parameter "K" and change in river gradient. (b–f) represent the changes of variables as a function of channel distance and graphed as box plots showing median, 25th and 75th percentiles; (d) illustrates the proportions of discordant ages. The box plots illustrate the range of values for each set: (b) sphericity (Ψ); (c) roughness; (e) apparent grain density; and (f) grain length and grain width.

longitudinal channel profile (Figure 6b). The variations in sphericity measures are controlled by differences in source material, i.e., an increase in grain sphericity from #13 to #15 that reflects the detrital intake of multi-cycled basin material from sedimentary rocks.

While sphericity of detrital grains is an important morphological characteristic in understanding depositional environments, imaging grain surfaces in 3-D and evaluating grain roughness better constrains the level of grain damage and links 3-D grain shape characteristics with U-Pb age distributions. The roughness increases in source regions with contributions from both the main channel and proximal sources. A decrease in grain surface roughness occurs during transportation within the basin due to mechanical abrasion from multi-cycled basin material. An increase of grain roughness in the vicinity of the Murchison Gorge is likely caused by new source material provided by the Northampton Complex (Figures 5b and 6c). The variations in roughness show how sensitive sample location and proximity to source material are for detrital grains in river samples. Overall, the change in roughness values displays a weak positive correlation with sphericity for samples #29 and #28, located in the main channel of the Murchison River within the Yilgarn Craton region, and a weak negative correlation for samples #13, #15 and #16, located further downstream (Figure 5b).

The proximity to bedrock source rocks is key in understanding roughness variations, and it appears that chemical abrasion, metamictization and metamorphic or metasomatic overgrowth are the dominant factors that influence roughness, before the source rocks get eroded, rather than subsequent river transport damage. An increase of sphericity and grain smoothness between #13 and #15 is likely caused by the introduction of multi-cycled detritus of basin material rather than mechanical abrasion caused by fluvial transport of the Murchison River.

The analysis of 3-D pit morphologies reveals a diversity of zircon grain damage, varying from shallow narrow tubes with pointy ends to wide areas with level bases (Figure 5c). Deep, bulgy pits are likely to present recrystallization textures, which were connected to the crystal surface, and may be related to local dissolution processes (Hoskin & Black, 2000). During river transport, mechanical abrasion appears to produce shallower and irregular surface areas (Figure 5c–green arrow) with prominent linear dents across the grains (Figure 5c–red arrow).

Metamict grains, typically recognizable in U-Pb data sets by their high degree of discordance (55%), occur in all river sand samples. Figure 7d illustrates the loss of metamict zircon grains relative to transport distance by a decrease of discordant data from #29 to #13 in the Yilgarn Craton region. In the basins however, multicycled, progressively "younger" age signatures of the sedimentary material are likely to contribute to an increase of hydrothermally or diagenetically altered zircon grains and therefore an increase in discordant data. While erosion at source continuously releases metamict zircon grains into the dynamic transport system of the river, the apparent density mean values increase continuously toward the outlet of the Murchison River (Figure 6e). Upstream river sand samples on average contain the least dense zircon grains, and apparent density increases near constantly relative to transport distance (Table 3). The increase of apparent density along the river channel occurs in spite of hydraulic sorting, which would predict that denser grains become less common with increasing channel length. We suggest that the near constant decrease of low-density zircon grains is due to lower mechanical strength of metamict grains and the resulting fragmentation of damaged grains as well as higher density, less metamict grains become more common in the system. This increase in median density in the upstream river system is documented clearly from #29 to #13, which contain similar age components. The constant increase in mean density in transport direction effectively is defined by a density increase rate of 0.05 g/cm^3 per 100 km channel length for a low river gradient of 0.25 m/km. Throughout the entire catchment area, density values of detrital zircons increase linearly with transport distance by a mean value of 0.03 g/cm^3 per 100 km, which is very similar to 0.027 g/cm^3 that we calculated from data of detrital zircon grains from the Frankland River published by Cawood et al. (2003).

3-D grain size distributions relate to transport distance, proximity to source material and river gradient, which most likely reflects the mature sorting system within the channel system. Larger grain sizes (length and width) occur at close proximity to source regions, the Yilgarn Craton – Capricorn Orogen basins and Northampton Complex with contributions from the main channel material. Smaller grain sizes are controlled by mechanical abrasion during transport through the Phanerozoic basins where multi-cycled basin material is mixed with main channel material. Here, the length of the grains decreases at a higher rate than

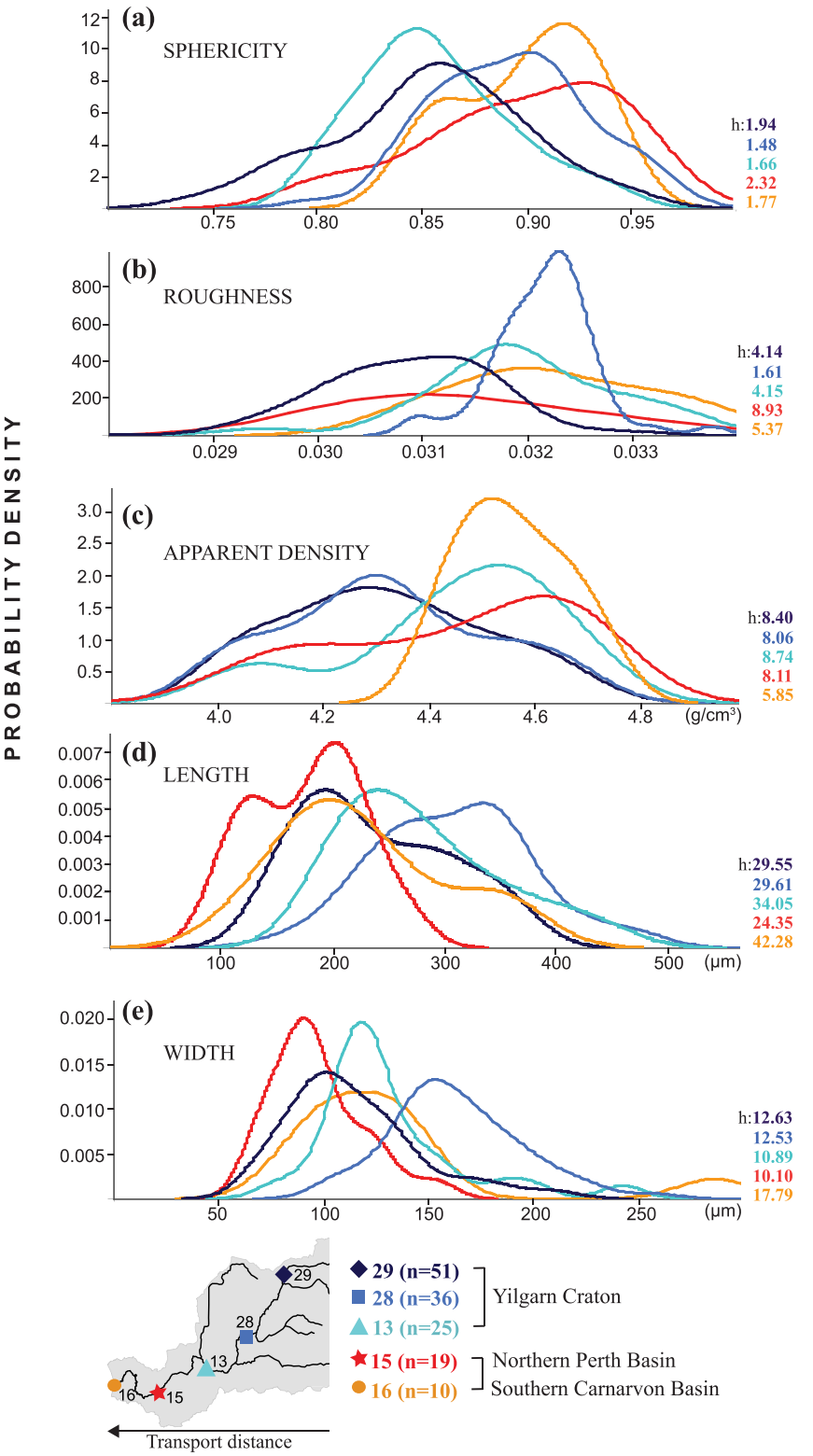

Figure 7. Kernel density estimation plots of Archean detrital zircon grains based on grain shape and size parameter and density variations in relation to transport distance. Range of measurements and amplitude variations of (a) Sphericity; (b) Roughness; (c) Apparent density; (d) *Length3d* and (e) *Width3d*. *Length3d* and *Width3d* represent Avizo measures. Each sample is colour coded and location is shown in the map. The bandwidth of the Gaussian kernels are shown for each curve to reflect local density of points.

grain width (Figure 6f). With the introduction of the Northampton Complex source, grain sizes increase, and larger Meso-Neoproterozoic zircon grains dominate the smaller Archean age population (Markwitz & Kirkland, 2017), amplified by an increase river gradient and hydraulic sorting.

4.4. 3-D Grain Shape Evolution Within Archean Detrital Zircon Population During Fluvial Transport

Archean detrital zircon grains are represented throughout all samples, including the Yilgarn Craton source region, in the basins, the Northampton Complex and at the outlet of the Murchison River in Kalbarri (Figure 6a). Therefore, Archean concordant grains were used to quantify grain shape, density and size evolution in relation to river transport distance and to compare the outcome to the overall results from sections 4.2 and 4.3 (Figure 7).

We report the change of zircon density during fluvial transport from apparent density calculations of the dose of alpha event by using U and Th concentrations and $^{206}Pb/^{207}Pb$ ages (after Murakami et al., 1991). The underlying assumption in this case is that radiation damage has affected the zircon grains ever since they crystallized. An alternative approach would be to assume that the apparent density is only affected by radiation damage that occurred after the grains cooled below the zircon partial annealing temperature (cf. Brandon et al., 1998; Rahn et al., 2004; Tagami et al., 1998). To test to what extent this assumption affects alpha dose, density and therefore grain shape evolution along transport, we recalculated the apparent density for the Archean population by an assuming a 500 Ma cooling age for the West Australian Craton. This age is estimated based on previously reported U-Pb disturbance ages in zircons at ca. 600 Ma in the Eastern Goldfields Superterrane (Kirkland et al., 2017), a zircon Raman radiation damage age of 420 $\pm$ 110 Ma (Pidgeon, 2014) from an Archean Darling Range granite (western part of the Yilgarn Craton), and a ca. 500 Ma from an East Pilbara Archean gneiss (Wiemer et al., 2017). Results from these density recalculations indicate similar trends to measures based on 206Pb/207Pb age and show a continuous increase of apparent density from 4.69 g/cm^3 in samples from the headwaters of the Murchison River to 4.74 g/cm^3 toward the outlet (Table 3). We can therefore conclude, that our grain density calculations and relationship with grain shape is essentially independent of the assumed age when alpha dose damage starts.

We observed that the range and amplitude of median values change in relation to sample location in the catchment and in relation to transport distance. The distribution of 3-D grain shapes is displayed using the kernel density estimation method as a set of Gaussian distributions for sphericity (Figure 7a), roughness (Figure 7b), apparent density (Figure 7c), grain length (Figure 7d) and width (Figure 7e). Sphericity of Archean detrital zircon grains is characterized by a wide range of values, nevertheless the general trends of grain sphericity maxima shift from lower values in the Yilgarn Craton to higher sphericity values in the basins in the fluvial transport direction (Figure 7a). New basement source material from the Yilgarn Craton itself, the Sandford River confluence, and the Northampton Complex is interpreted to "reset" the increasing sphericity trends over transport distance. Roughness measures display wide low probability peaks, with the exception of sample #28. Grain surfaces become smoother over transport distance, a feature likely influenced by proximal basement sources and multi-cycled basin material (Figures 6c and 7b). The range of apparent grain density is controlled by source ages and grain chemistry. We interpret this pattern to reflect mechanical abrasion removing damaged grains continuously during transport. The wide range of apparent grain density values are displayed as relatively flat peaks in the probability distributions for all samples, except for #16, which yields the highest density grains for all samples. At #16, shape and grain size trends are interpreted to have been reset by new source material from the Northampton Complex. Archean grain sizes (Figures 7d and 7e) show the same overall trend as discussed for median grain size variations of all age fractions in Figure 6f). Archean grain length and width variations are highly influenced by source variations, and generally decrease in size toward the outlet. The grain width distributions have narrower peaks than those for grain length, controlled by the size variation of the Archean source material and mechanical abrasion during transport. Significant change in slope, controlled by regional faults in the Murchison Gorge, appear not to have a significant effect on reduction of grain size (Figures 7d and 7e). On the contrary, grain sizes increase from #15 to #16 is likely due to hydraulic sorting by higher stream velocity, and new source material from basement rocks of the Northampton Complex.

Overall, the distribution range and peaks in the Archean detrital zircon data highlight the importance of 3-D grain shape analysis that documents the sensitivity of the river load to new detrital sources, channel slope and transport distance, even though overlapping influences of various source materials occur. There is an

important trend recognizable between basement source rock material and multi-cycled basin material. When samples are dominated by multi-cycle basin material (#15;16), a distinct increase of sphericity and smoother grains, which are generally smaller in length and width compared to Yilgarn Craton samples (#13), can be observed. On the contrary, when proximal basement source rocks are the main contributors to the detrital cargo (#29; #28: #13), grains are characteristically large, less rounded, and have rougher surfaces.

4.5. Detrital Zircon Age Components

The Narryer Terrane is known to be the oldest part of the Yilgarn Craton with zircon ages of up to 3.6 Ga (Sylvester et al., 2011) from Mount Murchison, 3.5 Ga to 3.7 Ga from Mount Narryer and adjacent gneissic rocks, and >4 Ga from the supracrustal rocks of Jack Hills (Wilde et al., 2001; see Figure 1 for location). Since river samples #28 and #29 are within close range of Mount Murchison and Mount Narryer, one would expect that these samples contain age signatures similar to the exposed bedrock in these areas. Importantly, detrital zircon analyses of #29 and #28, did not produce ages older than 3.54 Ga and 3.3 Ga respectively. Both samples contain dominantly Archean age components from the Yilgarn Craton south of the Narryer Terrane with ages between 2.6 and 3.1 Ga. None of the > 3.6 Ga ages are reflected in our data, similar to previous findings by Griffin et al. (2004), who also remarked the lack of this age group in stream samples. One possible explanation could be that the erosional denudation of Eoarchean bedrock in this region has occurred relatively recently and therefore the heavy mineral load of the source is not common in the drainage channels. A more likely explanation may be that Eoarchean and Hadean zircons are not present in our samples, because they are relatively rare.

5. Conclusion

We present the first X-ray tomography analysis in combination with U-Pb geochronology of detrital zircon grains from river sands of the Murchison River. We show that grain shape descriptors extracted from tomographic volumes and surfaces enable a complete three-dimensional documentation and quantification of grain shape evolution during fluvial transport. Zircon grain sphericity and roughness measures show a weak positive correlation with transport distance with a general trend of surface smoothing and rounding that in places is reset by the addition of new source material from crystalline basement and from multi-cycled basin material to the existing main channel load. 3-D zircon grain lengths and widths depend on transport distance, proximity to source material and river gradient. The erosional bias is affected by changes in river gradient, which in turn is controlled by faults and the recent uplift history in the Murchison Gorge as documented in zircon age populations across the samples. This leads to an underrepresentation of the Archean upstream sources at the outlet. We calculated a continuous increase of the mean apparent density of detrital zircon grains of 0.03 g/cm^3 per 100 km transport distance along the Murchison River, which we attribute to the apparent loss of metamict grains in the transport direction that highlights the selectiveness of detrital cargo in our samples. The rate by which the mean apparent density increases may be indicative of total channel length in similar river systems, as indicated by comparable values calculated from published data. We conclude that 3-D grain shape of detrital zircon carries meaningful information that can assist in evaluating preservation bias. We anticipate our method to be useful to better understand preservation bias in fluviatile transport systems in other continents and other tectonic settings.

Acknowledgments
VM thanks the Geological Survey of Western Australia (Exploration Incentive Scheme) for support in collection of the geochronology data. N. Evans and B. McDonald are thanked for assistance with analyses at the John de Laeter Centre for Mass Spectrometry at Curtin University (Perth). K. Gessner publishes with the permission of the Executive Director of the Geological Survey of Western Australia. A. I. S. Kemp is thanked for a thorough review of this manuscript. R. Ketcham and M. Ibanez-Mejia are thanked for their helpful comments and suggestions. All data necessary to understand, assess and extend our conclusions of the manuscript are attached. One of the original XRT volumes is available for download (doi:10.4225/23/59d34351f9bce).

References

Allègre, C. J., & Rousseau, D. (1984). The growth of the continent through geological time studied by Nd isotope analysis of shales. *Earth and Planetary Science Letters*, *67*, 19–34.

Andersen, T. (2005). Detrital zircons as tracers of sedimentary provenance: Limiting conditions from statistics and numerical simulation. *Chemical Geology*, *216*, 249–270.

Andò, S., Garzanti, E., Padoan, M., & Limonta, M. (2012). Corrosion of heavy minerals during weathering and diagenesis: A catalog for optical analysis. *Sedimentary Geology*, *280*, 165–178.

Barnett-Moore, N., Flament, N., Heine, C., Butterworth, N., & Müller, R. D. (2014). Cenozoic uplift of south Western Australia as constrained by river profiles. *Tectonophysics*, *622*, 186–197.

Brandon, M. T., Roden-Tice, M. K., & Garver, J. I. (1998). Late Cenozoic exhumation of the Cascadia accretionary wedge in the Olympic Mountains, northwest Washington State. *Geological Society of America Bulletin*, *110*, 985–1009.

Bruguier, O., Bosch, D., Pidgeon, R. T., Byrne, D. I., & Harris, L. B. (1999). U-Pb chronology of the Northampton Complex, Western Australia - evidence for Grenvillian sedimentation, metamorphism and deformation and geodynamic implications. *Contributions to Mineralogy and Petrology*, *136*, 258–272.

Buscombe, D. (2013). Transferable wavelet method for grain-size distribution from images of sediment surfaces and thin sections, and other natural granular patterns. *Sedimentology*, *60*, 1709–1732.
Cawood, P. A., Nemchin, A. A., Freeman, M. J., & Sircombe, K. (2003). Linking source and sedimentary basin: Detrital zircon record of sediment flux along a modern river system and implications for provenance studies. *Earth and Planetary Science Letters*, *210*, 259–268.
Champion, D. C., & Cassidy, K. F. (2007). An overview of the Yilgarn Craton and its crustal evolution. *Geoscience Australia Record*, *14*, 8–13.
Condie, K. C., & Aster, R. C. (2009). Zircon age episodicity and growth of continental crust. *Eos, Transactions American Geophysical Union*, *90*, 364–365.
Corfu, F., Hanchar, J. M., Hoskin, P. W. O., & Kinny, P. (2003). Atlas of Zircon Textures. *Reviews in Mineralogy and Geochemistry*, *53*, 469–500.
Cox, M. R., & Budhu, M. (2008). A practical approach to grain shape quantification. *Engineering Geology*, *96*, 1–16.
Dodson, M. H., Compston, W., Williams, I. S., & Wilson, J. F. (1988). A search for ancient detrital zircons in Zimbabwean sediments. *Journal of the Geological Society London*, *145*, 977–983.
Embleton, B. J. J., & Schmidt, P. W. (1985). Age and significance of magnetizations in dolerite dykes from the Northampton Block, Western Australia. *Australian Journal of Earth Sciences*, *32*, 279–286.
Ewing, R. C., Meldrum, A., Wang, L. M., Weber, W. J., & Corrales, L. R. (2003). Radiation damage in zircon. In: J. M. Hanchar & P. W. O. Hoskin (Eds.), *Zircon, Reviews in mineralogy and geochemistry* (Vol. 53, pp. 387–425). Mineralogical Society of America.
Farr, T. G., Rosen, P. A., Caro, E., Crippen, R., Duren, R., Hensley, S., . . . Alsdorf, D. (2007). The shuttle radar topography mission. *Reviews of Geophysics*, *45*, RG2004. https://doi.org/10.1029/2005RG000183
Fedo, C. M., Sircombe, K. N., & Rainbird, R. H. (2003). Detrital zircon analysis of the sedimentary record. *Reviews in Mineralogy and Geochemistry*, *53*, 277–303.
Gardiner, N. J., Kirkland, C. L., & Van Kranendonk, M. J. (2016). The Juvenile Hafnium isotope signal as a record of supercontinent cycles. *Scientific Reports*, *6*, 38503.
Garzanti, E., Andò, S., & Vezzoli, G. (2008). Settling equivalence of detrital minerals and grain-size dependence of sediment composition. *Earth and Planetary Science Letters*, *273*, 138–151.
Gehrels, G. (2014). Detrital zircon U-Pb geochronology applied to tectonics. *Annual Review of Earth and Planetary Sciences*, *42*, 127–149.
Griffin, W. L., Belousova, E. A., Shee, S. R., Pearson, N. J., & O'reilly, S. Y. (2004). Archean crustal evolution in the northern Yilgarn Craton: U–Pb and Hf-isotope evidence from detrital zircons. *Precambrian Research*, *131*, 231–282.
Hawkesworth, C., Cawood, P., Kemp, T., Storey, C., & Dhuime, B. (2009). A matter of preservation. *Science*, *323*, 49–50.
Hocking, R. M. (1987). *Sedimentology and basin architecture of the Silurian Tumblagooda Sandstone, Perth-Carnarvon Basin, Western Australia* (126 p.). Armidale, NSW: University of New England.
Hoskin, P. W. O., & Black, L. P. (2000). Metamorphic zircon formation by solid-state recrystallization of protolith igneous zircon. *Journal of Metamorphic Geology*, *18*, 423–439.
Hyslip, J. P., & Vallejo, L. E. (1997). Fractal analysis of the roughness and size distribution of granular materials. *Engineering Geology*, *48*, 231–244.
Iizuka, T., Komiya, T., Rino, S., Maruyama, S., & Hirata, T. (2010). Detrital zircon evidence for Hf isotopic evolution of granitoid crust and continental growth. *Geochimica et Cosmochimica Acta*, *74*, 2450–2472.
Jakica, S., Quigley, M., Sandiford, M., Clark, D., Fifield, K., & Alimanovic, A. (2011). Geomorphic and cosmogenic nuclide constraints on escarpment evolution in an intraplate setting, Darling Escarpment, Western Australia. *Earth Surface Processes and Landforms*, *36*, 449–459.
Kaminsky, W. (2007). From ClF to virtual morphology using the WinXMorph program. *Journal of Applied Crystallography*, *40*, 382–385.
Kemp, A. I. S., Wilde, S. A., Hawkesworth, C. J., Coath, C. D., Nemchin, A., Pidgeon, R. T.,. . . DuFrane, S. A. (2010). Hadean crustal evolution revisited: New constraints from Pb–Hf isotope systematics of the Jack Hills zircons. *Earth and Planetary Science Letters*, *296*, 45–56.
Ketcham, R. A. (2005). Three-dimensional grain fabric measurements using high-resolution X-ray computed tomography. *Journal of Structural Geology*, *27*, 1217–1228.
Kiderlen, M., & Meschenmoser, D. (2009). Error bounds for surface area estimators based on Crofton's formula. *Image Analysis & Stereology*, *28*, 165–177.
Kirkland, C. L., Abello, F., Danišík, M., Gardiner, N. J., & Spencer, C. (2017). Mapping temporal and spatial patterns of zircon U-Pb disturbance: A Yilgarn Craton case study. *Gondwana Research*, *52*, 39–47.
Košler, J., Sláma, J., Belousova, E., Corfu, F., Gehrels, G. E., Gerdes, A., . . . Woodhead, J. D. (2013). U-Pb detrital zircon analysis-results of an inter-laboratory comparison. *Geostandards and Geoanalytical Research*, *37*, 243–259.
Ksienzyk, A. K., Jacobs, J., Boger, S. D., Kosler, J., Sircombe, K. N., & Whitehouse, M. J. (2012). U-Pb ages of metamorphic monazite and detrital zircon from the Northampton Complex: Evidence of two orogenic cycles in Western Australia. *Precambrian Research*, *198–199*, 37–50.
Lancaster, P. J., Storey, C. D., Hawkesworth, C. J., & Dhuime, B. (2011). Understanding the roles of crustal growth and preservation in the detrital zircon record. *Earth and Planetary Science Letters*, *305*, 405–412.
Lawrence, R. L., Cox, R., Mapes, R. W., & Coleman, D. S. (2011). Hydrodynamic fractionation of zircon age populations, *GSA Bulletin*, *123*, 295–305.
Legland, D., Arganda-Carreras, I., & Andrey, P. (2016). MorphoLibJ: Integrated library and plugins for mathematical morphology with ImageJ. *Bioinformatics*, *32*, 3532–3534.
Link, P. K., Fanning, C. M., & Beranek, L. P. (2005). Reliability and longitudinal change of detrital-zircon age spectra in the Snake River system, Idaho and Wyoming: An example of reproducing the bumpy barcode. *Sedimentary Geology*, *182*, 101–142.
Malusa, M. G., Carter, A., Limoncelli, M., Villa, I. M., & Garzanti, E. (2013). Bias in detrital zircon geochronology and thermochronometry. *Chemical Geology*, *359*, 90–107.
Markwitz, V., & Kirkland, C. L. (2017). Source to sink zircon grain shape: Constraints on selective preservation and significance for Western Australian Proterozoic basin provenance. *Geoscience Frontiers*, 10.1016/j.gsf.2017.04.004.
Markwitz, V., Kirkland, C. L., & Evans, N. J. (2017a). Early Cambrian metamorphic zircon in the northern Pinjarra Orogen: Implications for the structure of the West Australian Craton margin. *Lithosphere*, *9*, 3–13.
Markwitz, V., Kirkland, C. L., Wyrwoll, K.-H., Hancock, E. A., Evans, N. J., & Lu, Y. J. (2017b). Variations in zircon provenance constrain age and geometry of an Early Paleozoic rift in the Pinjarra Orogen, East Gondwana. *Tectonics*, *36*. https://doi.org/10.1002/2017TC004696
Mazzullo, J., Sims, D., & Cunningham, D. (1986). The effects of eolian sorting and abrasion upon the shapes of fine quartz sand grains. *Journal of Sedimentary Petrology*, *56*, 45–56.
McWhae, J. R. H., Playford, P. E., Lindner, A. W., Glenister, B. F., & Balme, B. E. (1956). The stratigraphy of western Australia. *Journal of the Geological Society of Australia*, *4*, 1–153.

Moecher, D. P., & Samson, S. D. (2006). Differential zircon fertility of source terranes and natural bias in the detrital zircon record: Implications for sedimentary provenance analysis. *Earth and Planetary Science Letters*, *247*, 252–266.
Murakami, T., Chakoumakos, B. C., Ewing, R. C., Lumpkin, G. R., & Weber, W. J. (1991). Alpha-decay event damage in zircon. *American Mineralogist*, *76*, 1510–1532.
Nutman, A. P., Bennett, V. C., Kinny, P. D., & Price, R. (1993). Large-scale crustal structure on the northwestern Yilgarn Craton, Western Australia: Evidence from Nd isotopic data and zircon geochronology. *Tectonics*, *12*, 971–981.
Occhipinti, S., Hocking, R., Lindsay, M., Aitken, A., Copp, I., Jones, J., . . . Metelka, V. (2017). Paleoproterozoic basin development on the northern Yilgarn Craton, Western Australia. *Precambrian Research*, *300*, 121–140.
Paton, C., Hellstrom, J., Paul, B., Woodhead, J., & Hergt, J. (2011). Iolite: Freeware for the visualisation and processing of mass spectrometric data. *Journal of Analytical Atomic Spectrometry*, *26*, 2508–2518.
Pidgeon, R. T. (2014). Zircon radiation damage ages. *Chemical Geology*, *367*, 13–22.
Pirajno, F., & Occhipinti, S. A. (2000). Three Palaeoproterozoic basins - Yerrida, Bryah and Padbury - Capricorn Orogen, Western Australia. *Australian Journal of Earth Sciences*, *47*, 675–688.
Pupin, J. P. (1980). Zircon and granite petrology. *Contributions to Mineralogy and Petrology*, *73*, 207–220.
Pye, W. D., & Pye, M. H. (1943). Sphericity determinations of pebbles and sand grains. *Journal of Sedimentary Petrology*, *13*, 28–34.
Rahn, M. K., Brandon, M. T., Batt, G. E., & Garver, J. I. (2004). A zero-damage model for fission-track annealing in zircon. *American Mineralogist*, *89*, 473–484.
Schindelin, J., Arganda-Carreras, I., Frise, E., Kaynig, V., Longair, M., Pietzsch, T., . . . Cardona, A. (2012). Fiji: An open-source platform for biological-image analysis. *Nature Methods*, *9*, 676–682.
Scoates, J. S., & Chamberlain, K. R. (1995). Baddeleyite (ZrO2) and zircon (ZrSiO4) from anorthositic rocks of the Laramie anorthosite complex, Wyoming: Petrologic consequences and U-Pb ages. *American Mineralogist*, *80*, 1317–1327.
Shaanan, U., & Rosenbaum, G. (2016). Detrital zircons as palaeodrainage indicators: Insights into southeastern Gondwana from Permian basins in eastern Australia. *Basin Research.* https://doi.org/10.1111/bre.12204
Sheppard, S., Occhipinti, S. A., & Tyler, I. M. (2003). The relationship between tectonism and composition of granitoid magmas, Yarlarweelor Gneiss Complex, Western Australia. *Lithos*, *66*, 133–154.
Sircombe, K. N. (2000). Quantitative comparison of large sets of geochronological data using multivariate analysis: A provenance study example from Australia. *Geochimica et Cosmochimica Acta*, *64*, 1593–1616.
Sircombe, K. N., Bleeker, W., & Stern, R. A. (2001). Detrital zircon geochronology and grain-size analysis of a ~2800 Ma Mesoarchean proto-cratonic cover succession, Slave Province, Canada. *Earth and Planetary Science Letters*, *189*, 207–220.
Sircombe, K. N., & Stern, R. A. (2002). An investigation of artificial biasing in detrital zircon U-Pb geochronology due to magnetic separation in sample preparation. *Geochimica et Cosmochimica Acta*, *66*, 2379–2397.
Sláma, J., & Košler, J. (2012). Effects of sampling and mineral separation on accuracy of detrital zircon studies. *Geochemistry, Geophysics, Geosystems*, *13*, Q05007. https://doi.org/10.1029/2012GC004106
Soille, P. (2013). *Morphological image analysis: Principles and applications*. Springer Science & Business Media. https://doi.org/10.1007/978-3-662-05088-0
Sternberg, S. R. (1986). Grayscale morphology. *Computer Vision, Graphics, and Image Processing*, *35*, 333–355.
Sylvester, P. J., Souders, A. K., & Myers, J. S. (2011). The record of early crustal evolution preserved in detrital zircons from Mount Murchison metasedimentary rocks, Western Australia, *Geological Society of America Annual Meeting*, *43*(5), 44.
Tagami, T., Galbraith, R., Yamada, F. R., & Laslett, G. M. (1998). Revised annealing kinetics of fission tracks in zircon and geological implications. In: P. Van den haute & F. De Corte (Eds.), *Advances in fission-track geochronology* (pp. 99–112). New York: Springer.
Vermeesch, P. (2004). How many grains are needed for a provenance study?. *Earth and Planetary Science Letters*, *224*, 441–451.
Vermeesch, P. (2012). On the visualisation of detrital age distributions. *Chemical Geology*, *312–313*, 190–194.
Voice, P. J., Kowalewski, M., & Eriksson, K. A. (2011). Quantifying the timing and rate of crustal evolution: Global compilation of radiometrically dated detrital zircon grains. *The Journal of Geology*, *119*, 109–126.
Wadell, H. (1935). Volume, shape, and roundness of quartz particles. *The Journal of Geology*, *43*(3), 250–280.
Wang, L. B., Frost, J. D., & Lai, J. S. (2004). Three dimensional digital representation of granular material microstructure from X-ray tomography imaging. *Journal of Computing in Civil Engineering*, *18*, 28–35.
Wiemer, D., Allen, C. M., Murphy, D. T., & Kinaev, I. (2017). Effects of thermal annealing and chemical abrasion on ca. 3.5Ga metamict zircon and evidence for natural reverse discordance: Insights for U-Pb LA-ICP-MS dating. *Chemical Geology*, *466*, 285–302.
Wilde, S. A., Valley, J. W., Peck, W. H., & Graham, C. M. (2001). Evidence from detrital zircons for the existence of continental crust and oceans on the Earth 4.4 Gyr ago. *Nature*, *409*, 175–178.
Young, R. W. (1986). Sandstone terrain in a semi-arid littoral environment: The Lower Murchison Valley, Western Australia. *Australian Geographer*, *17*, 143–153.